1

Buckling-Induced Origami Assembly of 3D Micro/Nanostructures: Designs, Materials, and Applications

Xu Cheng and Yihui Zhang

Tsinghua University, Applied Mechanics Laboratory, Department of Engineering Mechanics; Center for Flexible Electronics Technology, No. 1, Qinghua Yuan, Haidian District, Beijing 100084, People's Republic of China

1.1 Introduction

With the rapid development of micro/nano-fabrication technologies in recent years, the fundamental research on nanomembranes [1–8] and their applications in various fields, such as electronics/optoelectronics [3, 8, 9], micro/nano-electromechanical systems (MEMS/NEMS) [6, 10] and optics [11, 12], has become an area with enormous potentials and opportunities. Meanwhile, nanomembrane technologies are gradually deepening into people's daily life in extensive ways and play an increasingly important role in the development of modern intelligent society. For example, the microelectronics based on nanomembrane technologies (e.g. cell phones, laptops, and wearable devices), which serve as physical carriers of vital signal acquisition and transmission in artificial intelligence technologies, are integrated with more and more functionalities, with constantly decreasing sizes [13, 14]. However, the applications of the nanomembrane in microelectronics mostly focused on the two-dimensional (2D) micro/nanostructures and planar devices. The 2D layouts of nanomembranes may not be conducive to realizing further performance improvement or fulfilling specific crucial requirements in some scenarios [13, 15–17], such as the spatial light modulation [18], unconventional near field communication (NFC) with high Q factors [19, 20], and high-efficiency energy harvesters [21]. Development of techniques to transform nanomembranes into 3D micro/nanostructures could bypass some of the challenges encountered in the planar designs, providing a feasible route to achieve more diversity in device designs, better performance, and more advanced functionalities [22, 23]. However, many technological challenges existed in the fabrication of 3D micro/nanostructures [24]. Extensive efforts have been devoted to the development of new manufacturing methods in the past decades, and significant progress has been made in 3D nanomembrane fabrications. Of these methods, the 2D-to-3D assembly methods stand out and have received broad attention due to their inherent advantages, such as the excellent compatibility with modern planar fabrication

Nanomembranes: Materials, Properties, and Applications, First Edition.
Edited by Yongfeng Mei, Gaoshan Huang, and Xiuling Li.

technologies (e.g. lithography, deposition, and etching) and the extensive material applicability [22, 23]. Most of the existing 3D assembly methods can be categorized into four main classes based on their different loading/deformation characteristics, including the rolling, folding, curving, and buckling methods [23].

The rolling and folding methods rely on intrinsic gradient stresses (e.g. the heteroepitaxial crystalline bilayers [25, 26], nonepitaxially deposited nanomembranes [27], and ion–solid interactions [28, 29]) or extrinsic driving forces (e.g. capillary forces [30–32], magnetic forces [33, 34], and cell traction forces [35]) to assemble 2D nanomembranes into 3D micro/nanostructures, through global bending deformations and bendable hinge deformations, respectively. The feature of bending-dominated mode facilitates the formation of 3D micro/nanostructures with cylindrical and polyhedral geometries and their variants [36, 37] (e.g. tubular, helical, hexahedral, and dodecahedral), but it also limits the applications to other complex configurations. The curving methods mainly focus on integrating the 2D membranes onto nonplanar substrates [38–41] (e.g. convex/concave paraboloid surfaces, cylindrical surface, and spherical surfaces) through efficient transfer-printing methods (e.g. prestretching methods [42, 43], hydroprinting methods [44, 45], vacuum-assisted transfer printing [46], punch methods [47], and hierarchical stamp methods [48]). This type of method requires an accurate positioning of the nanomembrane components with respect to the target nonplanar substrate. The buckling methods introduce the soft elastomer substrates to serve as the assembly platform, which provides driving forces to trigger mechanical buckling deformations of 2D membrane precursors [22, 23].

A schematic illustration in Figure 1.1 shows the buckling-induced assembly process, which is composed of three main steps, including the fabrication of 2D precursors, transfer-printing process, and compressive buckling assembly [23, 49, 50]. Specifically, the nanomembrane structures were first fabricated on a source wafer

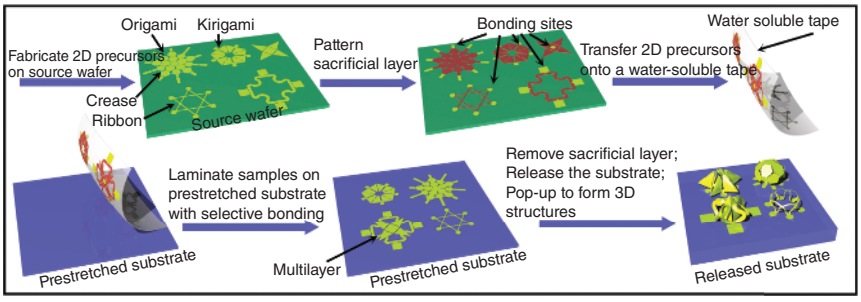

Figure 1.1 Schematic illustrations of origami assembly process of micro/nanostructures guided by controlled buckling. The process begins with transferring the 2D precursor structures with sacrificial layers and bonding sites, fabricated by advanced planar processing technologies, onto a water-soluble tape, followed by laminating the samples on a prestretched substrate with selective bondings. Removing the sacrificial layer and popping up the 3D microstructures by releasing the prestretched substrate completes the buckling assembly process. Source: Adapted with permission from Cheng and Zhang [23]. Copyright 2019, Wiley-VCH.

(e.g. sheet of monocrystalline silicon or glass) by modern planar manufacturing technologies, including lithography, deposition, and etching generally. Then, the bonding sites and the sacrificial layers were defined selectively through the electron beam (E-beam) evaporation technologies or magnetron sputtering technologies. In the transfer-printing process, a soft polydimethylsiloxane (PDMS) stamp or a water-soluble tape was exploited to transfer the 2D precursors onto the top surface of a prestretched elastomer substrate, followed by the ultraviolet (UV) light and heating treatments to activate the robust covalent bondings between the silicon dioxide layers on the bonding sites and the elastomer substrate. In the last step, releasing the prestretched substrate induces driving forces at the bonding sites, transforming the 2D precursors through spatial folding or coupled bending/twisting deformations and complex translational/rotational motions into target 3D geometries.

By introducing various design strategies on the patterned 2D precursors [19, 49, 51, 52], elastomer substrates [53–55], and paths of strain release [56, 57], a diversity of complex 3D geometries with wide-spanning length scales (e.g. from nanometers to millimeters) have been achieved. Furthermore, the integration of broad-ranging advanced functional materials (e.g. from typical rigid materials to newly emerging soft active materials) with the 3D micro/nanostructures has spawned compelling applications not only in electronics [58, 59], robotics [60], and sensors [61–63], but also in biomedical devices [64, 65], efficient energy harvesters [66, 67], and optics [55, 68].

This chapter aims to offer a comprehensive review of the latest progress of the aforementioned buckling-induced origami assembly methods, highlighting the design strategies, material integrations, and applications. It begins with the discussions on the buckling-induced folding assembly methods in Section 1.2, followed by the introduction to buckling-induced bending/twisting assembly in Section 1.3. The integration of advanced functional materials with 3D micro/nanostructures and the typical applications are summarized in Sections 1.4 and 1.5, respectively. Finally, an outlook on the existing challenges and future opportunities is provided.

1.2 Buckling-Induced Folding Assembly

The 3D micro/nanostructures induced by the folding methods typically contain creases with much lower stiffness than the other regions. In the buckling-induced folding assembly, it is essential to develop design strategies that can enable localized bending deformations at the crease regions without failure. This section discusses three representative folding strategies and their principles, including nonuniform thickness strategy [51], plasticity strategy [69], and loading path strategy [56].

1.2.1 Nonuniform Thickness Strategy

The thickness strategy realized folding creases in the 2D precursor structures through the spatial variation of thickness [51]. As shown in Figure 1.2a, a straight

ribbon, consisting of two panels (marked blue), two bonding sites (marked red), and three creases (marked gray), serves as an example to illustrate the design concepts and principles. The thickness (t_2) of creases is smaller than that (t_1) of panels, leading to negligible deformations in the panel parts, in the case of sufficiently small thickness ratio (t_2/t_1), because of the cubic downscaling of the bending stiffness with the nanomembrane thickness. Furthermore, another two key parameters controlling the folding angle are the prestretching strain (ε_{pre}) and the length ratio (L_2/L), where the L_2 and L are the lengths of creases and ribbons, respectively. The experimental and computational results in Figure 1.2a show that the folding angle of the straight ribbon increases with the increase of the length ratio and the prestrain (the middle and the bottom images in Figure 1.2a). In the folding assembly, it is important to avoid the fracture of the creases that accommodate most of the overall compressive deformation. Based on the finite element analysis (FEA) and the experimental verification, the maximum material strain in the creases can be effectively reduced by decreasing the thickness ratio and increasing the crease length. In addition to the accurate prediction of the folding assembly process through FEA methods, a theoretical solution for multi-segment thickness-varying structures can be obtained based on the classical elastica theory, which provides guidelines for the optimal design of folding structures [70].

The nonuniform thickness strategies can realize a broad set of versatile 3D mesostructures by elaborately designing the 2D precursors and crease patterns [51]. Figure 1.2b shows five representative mesostructures assembled through bidirectional or even hierarchical folding, including a "pyramid," a "windmill," a "cylindrical shell," a "car," and a "three-floor building with textured steps." It is noteworthy that these mesostructures are capable of reversible and deterministic control over the 2D-to-3D transformation by tuning the applied stretching strain on the elastomer substrate, due to the elastic nature of the assembly scheme.

1.2.2 Plasticity Strategy

The plasticity strategy provides an alternative and complementary method to 3D mesostructures with folding geometries, which relies on controlled plastic deformations of the 2D precursor structures [69]. Figure 1.2c illustrates the design concepts and principles through a straight ribbon structure with spatial variation of widths. According to the linear downscaling of the bending stiffness with the width of the straight ribbon, the sections with smaller widths are prone to out-of-plane bending deformation in the initial compression of the ribbon, causing plastic yielding of the metal. Furthermore, the plastic deformation exacerbates the stress concentration at the sections with smaller widths, leading to the well-designed creases as the valley and mountain folds during the 2D-to-3D transformation. In general, the reduction of widths and the strain localization-induced plastic deformations can dramatically decrease the bending stiffness at desired regions. As shown in the four experimental images of Figure 1.2c, the straight ribbon structure made of the metallic copper shows increasingly evident folding deformations as the prestrain (ε_{pre}) increases, while the straight ribbon structure made of the polyethylene glycol

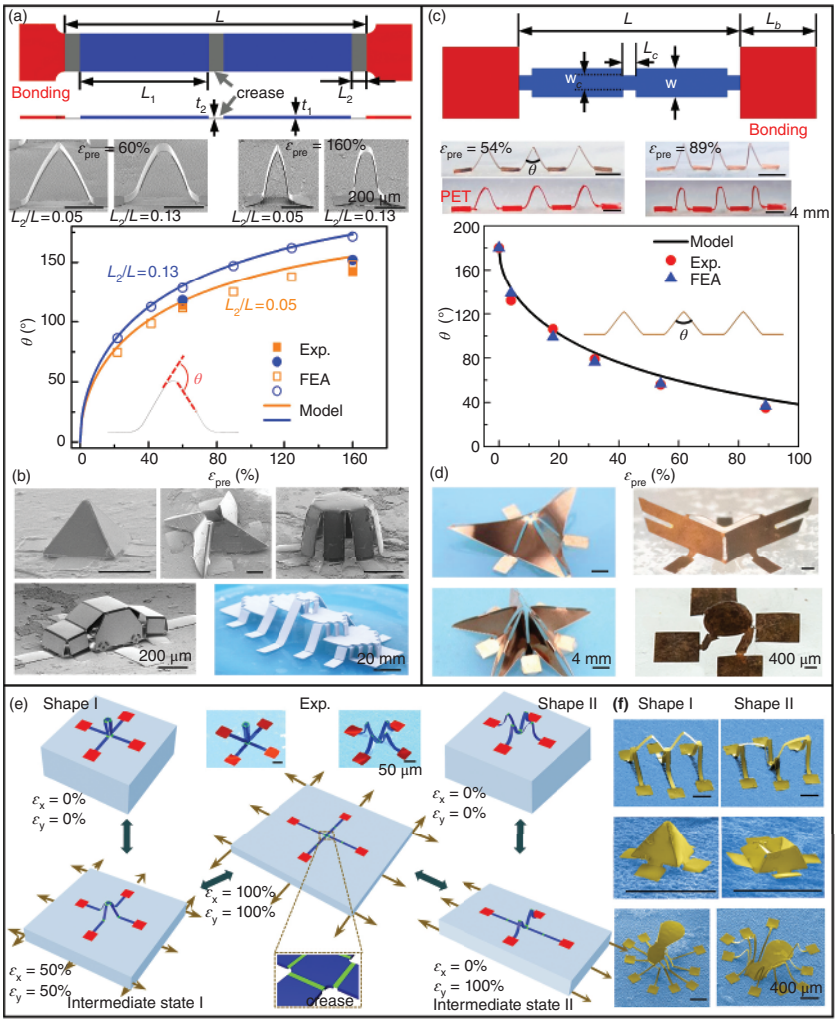

Figure 1.2 The 2D precursor design strategies and loading strategies of buckling-induced folding assembly. (a) Schematic illustrations of the nonuniform thickness strategy (top), SEM images of two deformed ribbons (made of bilayers of Au and SU8) with fixed thickness ratio and different length ratios under different prestrain levels (middle), and the folding angle (θ) versus the prestrain (ε_{pre}) for two straight ribbons with different length ratios (bottom). (b) Five representative examples of folding assembly of 3D mesostructures with nonuniform thicknesses. (c) Schematic illustrations of the plasticity strategy with nonuniform widths (top), optical images of two deformed ribbons (made of copper and PET, respectively) under two different levels of prestrain (middle), and the folding angle (θ) versus the prestrain (ε_{pre}) for the straight ribbon with a fixed thickness (bottom). (d) Four representative origami mesostructures based on the plasticity strategy. (e) Illustration of the reconfigurable folding assembly based on the loading path strategies through a sequence of FEA results and two SEM images. (f) SEM images of three representative reconfigurable origami mesostructures. Source: (a and b) Yan et al. [51]/with permission of John Wiley & Sons, Inc. (c and d) Shi et al. [69]/with permission of Elsevier. (e and f) Fu et al. [56]/with permission of Springer Nature.

terephthalate (PET) undergoes no obvious folding deformation due to the lack of plastic deformations. A dimensionless quantity (ρ_c/L_c) was defined to characterize the extent of folding deformations, where ρ_c is the ratio of minimum curvature radius in the crease region and L_c is the crease length. FEA results show that the critical prestrain (ε_c) triggering the evident folding deformations decreases under a given threshold (ρ_c/L_c) with the membrane thickness increasing. Besides, the folding angle (θ) decreases as the prestrain increases (Figure 1.2c, bottom), indicating that a larger prestrain (ε_{pre}) enables a more significant folding deformation.

Figure 1.2d highlights the use of the aforementioned folding strategy in several metallic 3D mesostructures, such as a "rotated table" and an "aircraft" [69]. In terms of the failure of metallic structures, the quantitative analyses relying on FEA show that the maximum material strain of the crease is in the range of 5–8%, which is well below the fracture threshold (~10%) of copper. It should be pointed out that the plasticity strategy is applicable not only to the 3D mesostructure made of metals, but also to diverse material systems by integrating a layer of metal on the designed 2D precursor structures.

1.2.3 Loading Path Strategy

The loading path strategy provides a practical route to reshape the folded 3D mesostructures reversibly by controlling the prestrain release paths of elastomer substrates [56]. Figure 1.2e shows the reversible process of shape change that involves the assembly of a 2D cross ribbon structure into two different stable 3D origami mesostructures with well-designed creases (marked green). The center of the cross structure was lifted to achieve the assembly of the column structure (Shape I) by synchronous release of the biaxial prestrain ($\varepsilon_x = \varepsilon_y = 100\,\% \rightarrow \varepsilon_x = \varepsilon_y = 0\%$). The sequential release of the x-direction prestrain ($\varepsilon_x = \varepsilon_y = 100\,\% \rightarrow \varepsilon_x = 0$, $\varepsilon_y = 100\%$) and the y-direction prestrain ($\varepsilon_x = 0$, $\varepsilon_y = 100\,\% \rightarrow \varepsilon_x = 0\,\%$, $\varepsilon_y = 0\%$) reshaped the column structure into the socket structure (Shape II). During the x-direction release process, the center of the cross ribbon was constrained by the ribbon along the y-direction, leading to the downward buckling mode of the final configuration. The fabrication of creases exploited the nonuniform thickness strategy and the creases played an important role in increasing the energy barrier between different stable configurations during the folding assembly. To analyze the bistability of the representative cross-shaped ribbon structure, a finite-deformation model based on the elastica theory and the perturbation method was established, providing guidelines for the designs of morphable folding structures [71].

Figure 1.2f shows three representative morphable mesostructures that can be reshaped between a "mountain" and a "valley," between a "pyramid" and a "swimming pool," and between an "octopus" and a "spider" [56]. It is important to point out that this strategy can also realize multiple stable geometries (>2) with well-designed release sequences by introducing various bistable elements (e.g. cross-shaped ribbons with creases) in the 2D precursor structures.

1.3 Buckling-Induced Bending/Twisting Assembly

The 3D micro/nanostructures induced by the bending/twisting method typically involve global bending and twisting deformations. The mode of bending and twisting deformations is mainly determined by the patterns of 2D precursor structures and the strain distributions of elastomer substrates. This section first introduces the deformation mode ratio [49] to characterize the bending and twisting deformation, and then discusses the principles of three representative design strategies, including kirigami design strategy [52, 72], multilayer design strategy [19], and engineered substrate strategies [53–55].

1.3.1 Deformation Mode Ratio

Filamentary structures typically consisting of slender thin ribbons (with the thickness and width much smaller than the width and arc length, respectively) represent a class of 3D mesostructures with combined bending and twisting deformations. The buckling of filamentary structures always involves considerable out-of-plane bending deformations. One practical approach to characterize the deformation components relies on a dimensionless quantity R, which is defined by the average twisting curvature (κ_{twist}) ratio to the average bending curvature (κ_{bend}) [49]. The deformation mode ratio varies drastically as the patterns of 2D precursor structure and bonding sites change. As shown in Figure 1.3a, the two representative mesostructures assembled from the same 2D precursor structures possess totally different deformation mode ratios, due to the different alignment of bonding sites [49]. The circular helix structure experiences similar levels of bending and twisting deformations ($R \approx 1.09$), while the flower-shaped structure mainly undergoes bending deformation ($R \approx 0.11$). By assuming the deformation mode of the helical structures and the frame structures, the analytical solutions can be established based on the principle of energy minimization [73, 74]. Furthermore, the deformed configurations for more extensive filamentary structures can be predicted by a double perturbation theory of postbuckling analyses [75].

Figure 1.3b shows two representative filamentary structures made of monocrystalline silicon [49]. Multilevel filamentary networks with combined bending and twisting deformations can be achieved by interconnecting multi-ribbons based on the mechanisms of hierarchical buckling.

1.3.2 Kirigami Design Strategy

The kirigami strategy relies on the strategically designed patterns of cuts to form the diverse 3D mesostructures with curved surfaces, achieving high levels of topographical complexity [52]. One of the advantages of the kirigami strategy is that the cuts change the load-transfer paths in the membrane during the compressive buckling process, with capabilities to reduce the stress concentration evidently and avoid the formation of folding creases. The top panel in Figure 1.3c serves as an example to

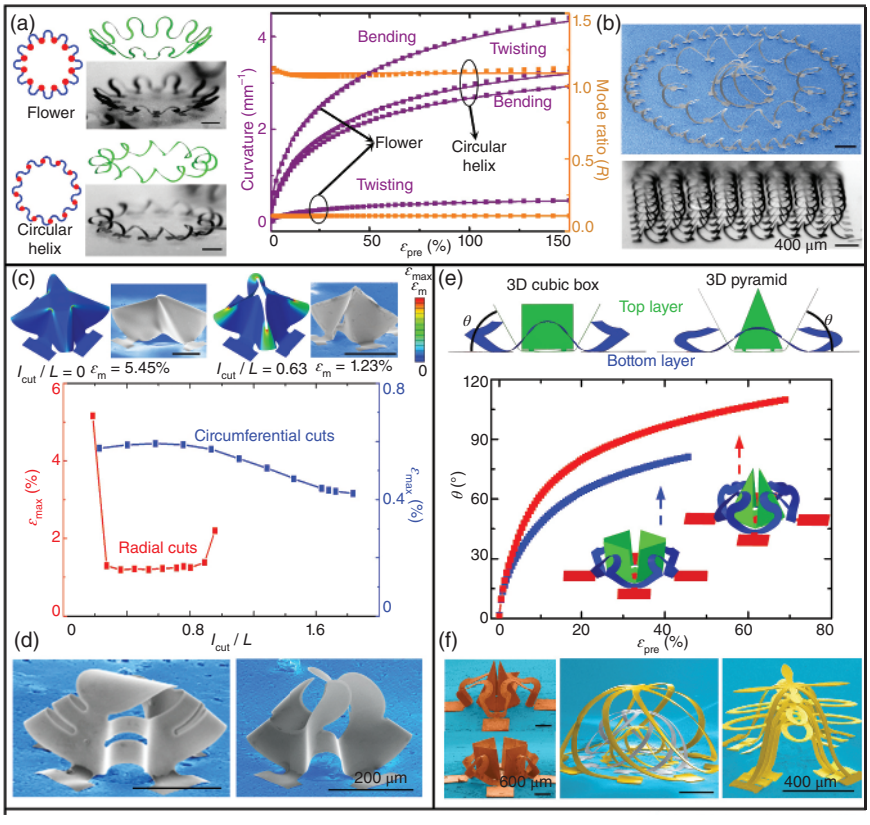

Figure 1.3 The 2D precursor and elastomer substrate design strategies of buckling-induced bending and twisting assembly. (a) Analyses of curvature components (bending and twisting) and mode ratio (R) for two representative filamentary mesostructures with the same 2D layout and different patterns of bonding sites. (b) SEM images of a complex circular helical structure (top) and a network of double-floor helices (bottom). (c) FEA results and SEM images of two mesostructures without and with radial cuts, and maximum material strain (ε_{max}) versus the dimensionless cut lengths (l_{cut}/L) for circular membranes. (d) Two representative kirigami mesostructures assembled with different kirigami patterns. (e) Computational results for the folding angle as a function of prestrain for the assembly of 3D cube and pyramid assisted by the lower ribbons. (f) SEM images of four unique multilayer 3D mesostructures. (g) Schematic illustrations of the buckling and twisting assembly of a morphable cross ribbon structure based on the kirigami substrates, and the rotation angles at the center of an individual square unit versus the applied biaxial strain. (h) SEM images of two representative mesostructures assembled on a typical kirigami elastomer substrate. Source: (a and b) Xu et al. [49]/with permission of American Association for the Advancement of Science – AAAS. (c and d) Zhang et al. [52]/with permission of National Academy of Sciences. (e and f) Yan et al. [19]/with permission of American Association for the Advancement of Science – AAAS. (g and h) Zhao et al. [55]/with permission of National Academy of Sciences.

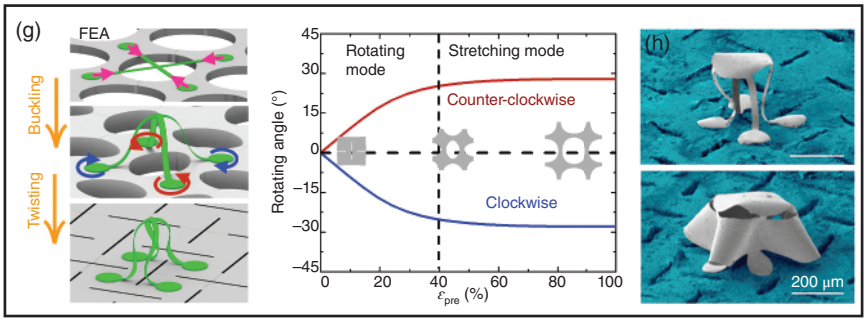

Figure 1.3 (*Continued*)

illustrate this advantage by comparing two mesostructures made of monocrystalline silicon with and without radial cuts. The corresponding FEA results show that the maximum material strain ($\varepsilon_m = 5.45\%$) in the mesostructure without cuts is much larger than that ($\varepsilon_m = 1.23\%$) of the structure with radial cuts due to the evident folding deformations. The bottom panel in Figure 1.3c shows the maximum material strain exhibits a nonlinear change with the increase of length ratio (l_{cut}/L), due to the influences of the cutting length on the deformation mode, where the l_{cut} and L are the length of cuts and the membrane, respectively.

Another advantage through use of this strategy is that the introduction of cuts enhances the design flexibility of 3D assembly in realizing 3D mesostructures with complex curved geometry. Figure 1.3d provides two representative mesostructures assembled from the same circular precursor geometries but tailored with different patterns of cuts [52]. The first symmetric kirigami mesostructure was achieved with the aid of cuts along the radial or circumferential directions, while the second antisymmetric mesostructure was induced by the cuts with serpentine patterns.

1.3.3 Multilayer Design Strategy

The multilayer design strategy provides a practical route to assemble multilayer 3D mesostructures with complex 3D topologies through the use of laminated and multilayer 2D precursors [19]. In the fabrication process of multilayer 3D mesostructures, releasable 2D precursor structures need to be transferred separately and stacked together on the prestretched elastomer substrate, thereby requiring precise positioning between different layers. Figure 1.3e shows two representative multilayer mesostructures leveraging the combined bending and twisting deformations of the bottom layer (e.g. ribbon structures) to drive the 3D folding assembly of the top layer (e.g. 3D cube and pyramid-like structure). The mechanical interactions between the two overlaying layers exerting contact forces at strategic locations can be well designed quantitatively by means of FEA. The computational results show that the folding angle and the contact forces increase as the prestrain increases, and gradually converge to a stable value. Besides, the driving forces can be transmitted over a relatively long distance by introducing a domino structure.

In addition to the above advantage, the multilayer strategy is capable of realizing densely distributed 3D architectures, which can be exploited to improve the functional and integration density at the device level. The mesostructures on the right of Figure 1.3f are examples (e.g. 3D trilayer nested cages and bionic trees) of densely distributed 3D structures. Other complex multilayer structures can be formed by entangling a plurality of ribbons and arranging the bonding sites of the upper layers on the underlying structures.

1.3.4 Engineered Substrate Strategies

The engineered substrate strategies rely precisely on tailored strain distributions of the elastomer platform to control the bending and twisting deformations of 3D mesostructures during buckling assembly. Three representative strategies have been proposed, including the engineered thickness strategy [54], engineered modulus strategy [53], and kirigami strategy [55].

The engineered thickness strategy tailors the distribution of substrate thickness through the casting and curing process of soft lithography [54]. Based on the linear downscaling of the tensile stiffness with the substrate thickness, the deformations in thick regions are much smaller than the thin regions, leading to much smaller out-of-plane deformations of 3D mesostructures. The inverse designs of the distributions of substrate strain and thickness relying on the iterative calculations of FEA can guide the assembly of unique 3D mesostructures (e.g. a 3D concave mirror-like structure and a 3D elevated helical coil).

The engineered modulus strategy is suitable for achieving strain distributions with larger strain ratios and larger strain gradients through the use of heterogeneous materials, in comparison to the engineered thickness strategy [53]. The heterogeneous substrates, typically prepared through multi-material 3D printing methods or casting and curing techniques, undergo much larger deformations in lower modulus regions and sharp strain variation in the material transition zone. Based on a finite deformation model, the strain distributions on the uniaxial substrate can be predicted and inversely designed. A variety of 3D mesostructures have been realized, including some biomimetic examples (e.g. a scorpion-like structure and a manta ray-like structure), which are not accessible through use of uniform substrates.

The kirigami designs of substrates introduce local twisting deformations into the assembly of 3D mesostructures through the use of interconnected, rotatable units [55]. The kirigami patterns fabricated by laser-cutting technology undergo large rotational motions with the applied prestretching strain. The cross-shaped ribbon structure in Figure 1.3g serves as an example to illustrate the deformation process of kirigami substrates. At the beginning stage of strain release in the substrate (stretching mode), the structure mainly undergoes out-of-plane buckling deformation ($40\,\% < \varepsilon_{\text{pre}} < 100\%$), followed by the twisting deformations when the substrate changes into the rotating dominated mode ($\varepsilon_{\text{pre}} < 40\%$). According to the FEA results, the rotation angle at the center of a square unit converges to a fixed value (e.g. ~30° for the square kirigami patterns) when the applied biaxial strain exceeds ~40%. Increasing the length of cut can effectively increase the rotation

angle of the square units, and, at the same time, increase the maximum material strain of the substrate. Therefore, a relatively large rotation angle can be obtained without fracture at the cutting regions by optimizing the ratio of the cut length to the length of the unit. Based on the nature of rotating features, a broad set of 3D mesostructures with local chiralities can be obtained. Figure 1.3h shows two representative 3D mesostructures based on the kirigami substrate. Besides, by incorporating the folding crease design and the loading path strategy with kirigami substrates, morphable 3D mesostructures with local chiralities can be constructed, further enhancing the design flexibility.

1.4 Functional Materials Integrated with 3D Mesostructures

The buckling-guided 3D assembly strategies apply very well to a wide range of advanced functional material systems, including but not limited to metallic materials, semiconductor materials, piezoelectric materials, 2D materials, and phase-change materials. The compatibility with diverse range of materials suggests a great potential in developing high-performance devices.

1.4.1 Metallic Conductors

The metallic materials (e.g. gold, copper, aluminum, nickel, and titanium) typically possess good ductility and good conductivity of heat and electricity, which can be integrated with 2D precursor structures conveniently through the E-beam evaporation technologies or magnetron sputtering technologies (Figure 1.4a) [49, 52]. Metallic materials integrated with the 3D mesostructures can function either as electrical interconnects [57, 65] or as coils to achieve electromagnetic signal transmissions [19, 79, 80] in two ways. Taking the recently proposed 3D strain sensor as an example, the two separate ribbons of the metallic spiral structure contact with each other at designed tensile strain, indicating the value of strain visually through the connected light-emitting diodes (LEDs) [57]. The 3D NFC device, assembled from a two-layered coil structure made of copper, has an enhanced Q factor and improved functional angle in comparison to the 2D counterparts [19].

1.4.2 Semiconductors

Semiconductor materials (e.g. silicon and GaAs) are widely used in microelectronic devices, which play an important role in the development of modern intelligent society. The buckling-induced origami assembly methods work well for monocrystalline silicon with a very small brittle fracture strain (~1%), by exploiting optimized geometrical parameters [22, 49]. The 3D high-density microelectronic devices can be realized by integrating large-scale chips on the 2D silicon precursors. Figure 1.4b shows two representative multilevel mesostructures made of monocrystalline silicon, where the material strain can be tailored by the FEA. Besides, the piezo-resistive

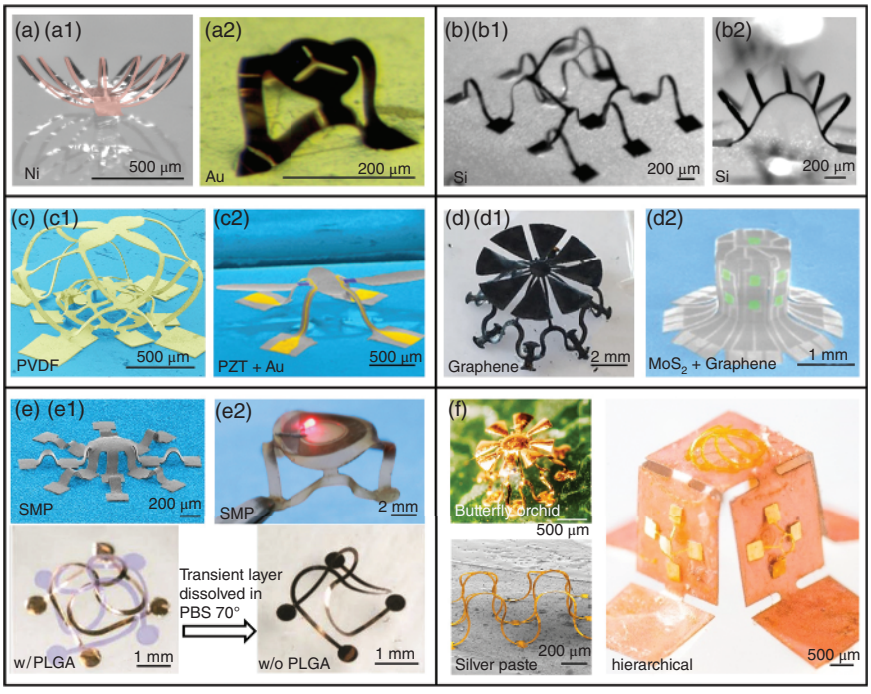

Figure 1.4 The integration strategies of advanced functional materials in the buckling-induced origami assembly. Representative 3D mesostructures integrating metallic conductors (e.g. Au, Ni in (a)), monocrystalline silicon (b), piezoelectric materials (e.g. PZT, PVDF in (c)), 2D materials (e.g. graphene, MoS_2 in (d)), and phase-change materials (e.g. SMP, PLGA in (e)). (f) Transfer printing of the buckled 3D origami mesostructures onto diverse substrates (e.g. butterfly orchid and silver paste) and hierarchical designs. Source: (a1and b1) Xu et al. [49]/with permission of American Association for the Advancement of Science – AAAS. (a2) Zhang et al. [52]/with permission of National Academy of Sciences. (c1) Han et al. [21]/with permission of Springer Nature. (c2) Ning et al. [61]/with permission of American Association for the Advancement of Science – AAAS. (d1) Ling et al. [76]/with permission of American Chemical Society. The right image in panel (d2) Lee et al. [68]/with permission of Springer Nature. (e1) Wang et al. [77]/with permission of John Wiley & Sons, Inc. (e2) Park et al. [78]/with permission of John Wiley & Sons, Inc. (f) Yan et al. [60]/with permission of National Academy of Sciences.

effect of silicon materials can also be exploited to design sensitive pressure sensors with multimodal responses (e.g. normal force, shear force, bending, and temperature) and relative wide dynamic range [81].

1.4.3 Piezoelectric Materials

There are two types of piezoelectric materials commonly used in buckling-induced origami assembly, including polyvinylidene difluoride (PVDF) [21] and $Pb(Zr_{0.52}Ti_{0.48})O_3$ (PZT) [61]. Their piezoelectric properties have a great potential for applications as 3D sensors and actuators. The left panel in Figure 1.4c shows an overlapping network made of the PVDF membrane [21]. The electrical signals

generated by the deformations of PVDF membranes can be collected by integrating metallic electrodes (e.g. Au) at strategic regions of the 3D mesostructure. Spin coating an eccentric layer (e.g. a polyimide [PI] layer) on the PVDF membrane can offset the sensing layer from the neutral mechanical plane, leading to an increase of the open-circuit output voltage by 2 orders of magnitude. The right panel in Figure 1.4c shows a fly-shaped mesostructure with a pair of mechanical actuators made of PZT nanomembrane on the wings [61]. The layouts of the PZT and metal electrodes are optimized by the quantitative FEA to ensure the material strain below the fracture strain (~0.6%). The deterministic control over the dynamical behavior and flapping resonate mode (resonant frequency ≈1.15 kHz) of 3D fly-shaped mesostructure relies on the strategically placed PZT microactuators on 3D geometries and the in-phase driving voltages applied to the actuators.

1.4.4 2D Materials

2D materials typically refer to the materials with electrons moving freely in a 2D plane at the nanometer scale (1–100 nm), such as the graphene and molybdenum disulfide (MoS_2) [68]. The left panel in Figure 1.4d shows a jellyfish-like mesostructure made of the CO_2 laser-induced cellular graphene [76]. Incorporation of the cellular graphene can form hierarchical mesostructures and greatly enhance the stretchability of cellular graphene while maintaining its excellent conductivity, which can hardly be achieved by its planar counterparts due to the irregularly distributed, porous microstructures. The 3D interdigital supercapacitors made of cellular graphene and solid-state electrolytes exhibit excellent electromechanical properties under the cyclic loading conditions. The right panel in Figure 1.4d shows an octagonal prism incorporating monolayer graphene (light gray) and MoS_2 (green), each of which provides an excellent combination of electrical, optical, and mechanical properties [68]. Specifically, graphene materials are suitable for use as flexible, transparent conductors and MoS_2 materials are of great interest for the excellent photovoltaic conversion properties. Such a heterogeneous material system can be used to fabricate high-performance 3D photodetectors with the aid of well-designed 3D geometries.

1.4.5 Phase-Change Materials

Introduction of phase-change materials into the 3D assembly methods can realize further actuations of as-assembled 3D mesostructures, allowing quick response to the environmental stimuli. The top panel in Figure 1.4e shows two representative mesostructures made of shape memory polymers (SMPs), a kind of soft active material, which can recover the initial 3D configurations under an external stimulus [77]. Cooling the heated mesostructures (~57 °C) to room temperature and maintaining the applied forces on the strategic locations of structures can fix the temporary geometries [77, 82]. This type of actuation can be realized either by directly heating the mesostructures or indirectly by light exposure of the mesostructures with embedded nanoparticles. Besides, with the use of SMPs, freestanding

3D mesostructures can be obtained by dissolving a sacrificial layer at bonding sites after the shape fixation (see the image at the top right of Figure 1.4e). The bottom panel in Figure 1.4e shows a 4D assembly process in which a 3D interwoven multilayer structure made of Cu/PI and poly(lactic-*co*-glycolic acid) (PLGA) bilayer was reshaped to a monolayer 3D mesostructure [78]. Exposing the assembled 3D mesostructures to specific environmental conditions, such as immersing the structures into phosphate-buffered saline solution (PBS) at 70 °C, can dissolve the transient layer and trigger the 4D assembly process, leading to the reconfiguration of geometries over time.

1.4.6 Transfer Printing of 3D Mesostructures

The elastomeric substrate provides supporting and driving forces for the assembly of 3D mesostructures, but it also limits the applications of these structures due to poor heat resistance, easy degradation, and other disadvantages [60]. Transfer-printing technologies allow the integration of assembled 3D mesostructures with nearly any class of platforms, greatly facilitating the practical applications in extensive environmental conditions. The transfer printing of 3D structures relies on a meltable wax, which starts with embedding the assembled 3D mesostructures in the wax, instead of the typically used soft stamps (e.g. PDMS) in planar fabrication process. Melting the wax (raising the ambient temperature) after printing on the desired substrate coated with a thin adhesive layer completes the process without changing 3D geometries of mesostructures. A set of 3D mesostructures (e.g. filamentary, kirigami, origami, multilayer, and hierarchical designs) on different target substrates (e.g. butterfly orchid, silver paste, quartz, chicken breast, and silicon) have been obtained (Figure 1.4f), exhibiting the versatility and flexibility of this transfer-printing strategy [60, 83].

1.5 Applications

1.5.1 Electronics

Figure 1.5a shows a concealable electromagnetic device capable of switching the working mode through shape change. The device consists of three planar antennas on the middle pad for wireless communication and an elastomeric substrate for assembly and support [56]. Based on the loading path strategy introduced in Section 1.2, the simultaneous release of the biaxial prestrain yields the working mode (Shape I) with antennas elevated to the top and high radiant efficiency due to the off state of electromagnetic shielding. Sequential release of the substrate strain leads to a concealing mode (Shape II) with low radiant efficiency, because of the metallic membrane structure shielding the three antennas. Figure 1.5b shows a deformable hemispherical electrically small antenna (ESA) with the meander line conducting paths, allowing large frequency bandwidths and relatively small physical sizes simultaneously [79]. The optimized inner interconnects under the ESA enable the approximation of non-developable hemisphere surface by eight

circumferentially distributed ribbons with variable widths. The 3D configuration can be easily reshaped by stretching or releasing the elastomeric substrate (ε_{appl}), providing a practical route to tune the frequency and normalized quality factor (Q/Q_{lb}) continuously and reversibly. Combined FEA results and experimental measurements showed that the best normalized quality factor occurs at strain-free state ($\varepsilon_{appl} = 0\%$) due to its hemispherical geometry. In addition to the 3D antennas, the 3D silicon electronic systems can also be fabricated by directly incorporating the high-performance n-channel silicon nanomembrane (Si NM) MOSFETs (n-channel metal oxide semiconductor [nMOS]) and p-channel Si NM MOSFETs (p-channel metal oxide semiconductor [pMOS]) into the assembled the 3D mesostructures [58].

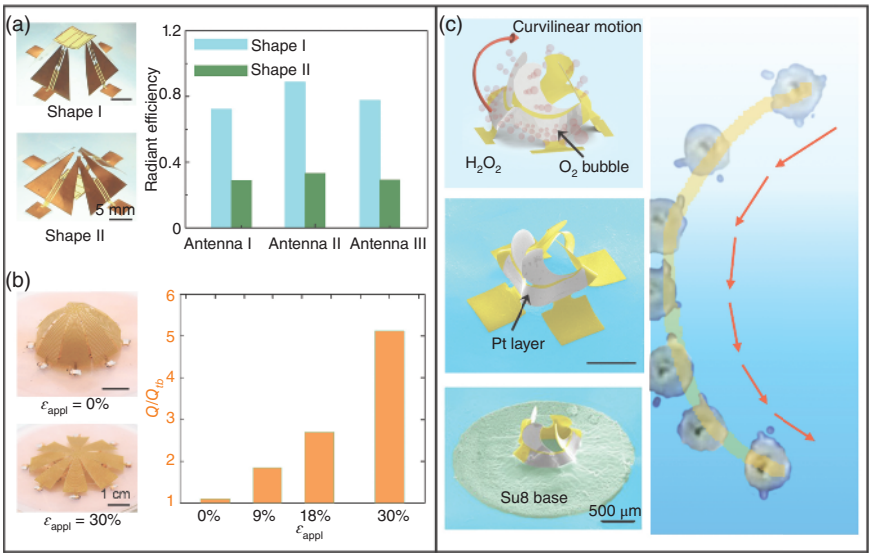

Figure 1.5 Applications of 3D mesostructures in electronics, robotics, sensors, and biomedical devices. (a) Optical images of the concealable electromagnetic device and the computational results of radiant efficiency at two different stable shapes (Shapes I and II) of the integrated three antennas. Source: Adapted with permission from Fu et al. [56]. Copyright 2018, Springer Nature. (b) Optical images of the hemispherical electrically small antenna under two different strain levels and the normalized quality factor (Q/Q_{lb}) versus applied stretching strain (ε_{appl}). Source: Liu et al. [79]/with permission of John Wiley & Sons, Inc. (c) Illustrations, SEM images, and super-imposed images of the 3D micro-swimmer with controlled motion modes and trajectories (the designed curvilinear motion). Source: Adapted with permission Yan et al. [60]. Copyright 2017, National Academy of Sciences. (d) The optical image of the impact-based 3D piezoelectric sensor and the time-domain output voltage by bending the encapsulated sensor along two vertical directions. Source: Adapted with permission from Han et al. [21]. Copyright 2019, Springer Nature. (e) A 3D fluid property sensor with five independently addressable PZT micro-actuators and the simulated resonant modes of the double-floor mesostructure (left). Measured and calculated viscosity of the water–glycerol mixtures with multiple mixing ratios (right). Source: Adapted with permission from Ning et al. [61]. Copyright 2018, AAAS. (f) Optical images of a health-monitoring device composed of helical network interconnects and the measured time-domain output signals of the electrophysiological recordings (e.g. EEG, EOG). Source: Jang et al. [65]/with permission of Springer Nature.

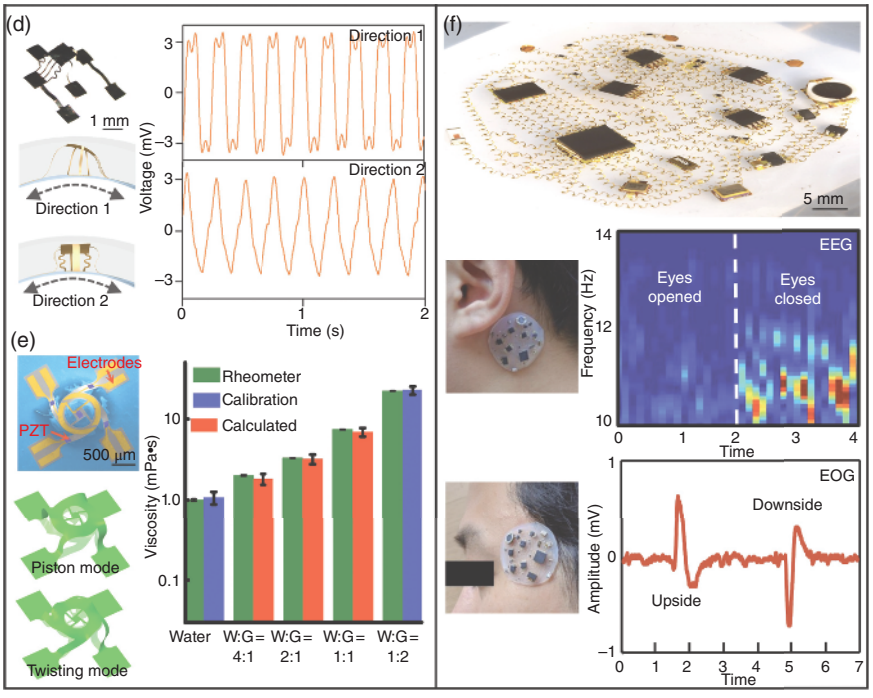

Figure 1.5 (*Continued*)

Systematic experimental and simulation studies on the 3D silicon electronic systems illustrated that the interconnected 3D bridges or coils ensure that the commercial transistors are not affected by external mechanical deformations (e.g. bending and shearing deformations) with negligible changes in transfer curves.

1.5.2 Robotics

Figure 1.5c shows 3D self-propelled micro-swimmers with controlled swimming modes and motion trajectories based on freestanding kirigami mesostructures [60]. The isolation of propeller-shaped mesostructure from the assembling substrate relies on the photocrosslinkable bases, which begins with dropping polymer liquids (e.g. SU8 droplets) onto the 3D mesostructures. The bonding sites can be constrained by a photodefined base with UV light radiation through a photomask. Besides, the freestanding mesostructures can also be obtained through the aforementioned SMPs [77], controlled plastic deformations, and mechanical interlocking systems [78]. Specifically, the plastic deformations of the thin metal films deposited in the 2D precursor fabrication process can maintain a certain amount of deformations instead of fully restoring the original 2D geometries. In this case, it is essential to take the springback effects into considerations to achieve precise geometric control of isolated mesostructures. The mechanical interlocking approach relies on well-designed mechanical interlocking elements consisting

of female-type lugs and male-type hooks. Irreversibly "lock-in" of the hooks and corresponding lugs along different directions (e.g. *x*-axis and *y*-axis) can be realized by controlling the loading paths. The strategically patterned nanomembranes of platinum (Pt, 100 nm in thickness) on the swimming robots are capable of catalyzing the hydrolysis of hydrogen peroxide (H_2O_2, 30% by weight), generating bubbles of O_2 at room temperature to propel the micro-swimmer in a controlled mode. Based on the multibody dynamics simulations and experimental results, the curvilinear motions rely on the Pt nanomembrane integrated on four petals and one side of the structure.

1.5.3 Sensors

Integrating piezoelectric materials (e.g. PVDF and PZT) with the 3D mesostructures implies attractive applications in MEMS/NEMS and sensors. Figure 1.5d shows impact-based 3D piezoelectric sensors encapsulated in a soft silicone elastomer, protecting the 3D device physically and maintaining its flexibility simultaneously [21]. One of the advantages of the 3D sensor is that the output voltage responses vary with the magnitude, applied location, and the applied direction of the mechanical stimuli. Under the bending mode of operation, the output voltage increases linearly as the curvature of the encapsulation elastomer increases. Besides, different bending directions (e.g. Directions 1 and 2) lead to distinguishable electrical signals with different voltage peaks. Figure 1.5e shows a fluid property sensor integrated with five independently addressable PZT nanomembranes [61]. Based on the well-tailored rotated-table geometry, the mesostructure has two qualitatively distinguished resonant modes (twisting motion and piston motion), the resonant frequencies of which have decoupled sensitivities to the viscosity and density of the fluids. A theoretical model of 3D vibrations has been established to offer guidelines for the measurement of fluid properties once the resonant frequencies of these working modes are known [84–86]. Compared with the experimental results based on a commercial rheometer, the calculated results based on the abovementioned principles exhibit good consistency for the water–glycerol mixtures. Besides, another 3D vibratory sensor driven by the Lorentz forces has been fabricated to measure the nanomembrane properties (e.g. modulus and density) based on the partially decoupled sensitivities of resonant frequencies in two distinct vibration modes [62].

1.5.4 Biomedical Devices

Figure 1.5f shows a stretchable health-monitoring device consisting of more than 50 electronic components (e.g. data storage/processing chips, capacitances, and sensors) interconnected by 3D open-mesh networks of helical microcoils [65]. Compared with the planar interconnects widely used in stretchable electronics (e.g. serpentine or fractal interconnects), the 3D helical mesostructures offer much higher levels of stretchability while maintaining the mechanical and electrical robustness, due to the reduction of stress concentration. Here, a two-stage encapsulation strategy was introduced to maximize the system-level stretchability of

the 3D health-monitoring device and protect the electronic components from the corrosions of water and oxygen [87]. Based on the detailed experimental results, this demonstrated device is capable of implementing reliable multifunctional operations for health monitoring, including 3D motion tracking, respiration monitoring, and electrophysiological signal monitoring (e.g. electrocardiograph [ECG], electromyography [EMG], electrooculogram [EOG], and electroencephalograph [EEG]). In addition to its application to health monitoring, the 3D micro/nanostructures can also be used as cell scaffolds to study the interactions of cell growth with the external environments. Systematic experimental results showed that the fibroblasts could adjust their alignments according to the geometries of 3D cell scaffolds. The fibroblasts exhibited highly ordered networks alignments on the 3D helical structures, while random and messy alignments on the 3D table-shaped structures [64]. Besides, introducing addressable microelectrodes into 3D cellular scaffolds enables the recording of electrophysiological signals of dorsal root ganglion (DRG) neural cells [60].

1.5.5 Energy Harvesters

Figure 1.6a shows a thermoelectric energy harvester composed of an array of compliant and stretchable helical microcoils [66]. The 3D helical geometries, integrating silicon ribbons with p-type and n-type segments at the coil legs, allow large temperature gradients across the thermoelectric device and low thermal impedance interfaces to the ambient flowing air. Introducing an encapsulation layer on the coil legs can enhance the heat flow through the legs and increase the total surface cooling capacity, exemplified by 9.7 nW increase in silicon heat flow. The experimentally measured output characteristics of the thermoelectric harvester satisfy the design expectations with good power outputs ($\approx$2 nW). Figure 1.6b shows a 3D piezoelectric energy harvester with an ultralow-stiffness serpentine design [21, 88]. To avoid the influence of interface adhesion [89] on the configuration of the ultralow-stiffness serpentine structure, a sacrificial structure was introduced in the buckling assembly process. The property of ultralow stiffness ensures particularly high sensitivity to low-frequency vibrations at small scale (in-plane size $\approx$1 mm). Implanting the piezoelectric energy harvester into the hind leg of a mouse, the bioenergy generated by mouse activity, including but not limited to trotting and climbing, can be converted into electrical energy, inducing more than 1 mV output voltages. The third recently reported energy harvester based on the buckling-induced 3D assembly is a graphene hygroelectric generator [67], which is capable of harvesting the chemical potential energy. By exposing the 3D pyramid-shaped hygroelectric generator to a moisture environment, the stable electricity output can be realized even under extreme deformations, such as uniaxially/biaxially stretching and out-of-plane compression.

1.5.6 Optical Devices

Figure 1.6c shows a mechanically tunable optical chiral metamaterial [55]. Controlled release of the kirigami substrate allows access to two reconfigurable 3D

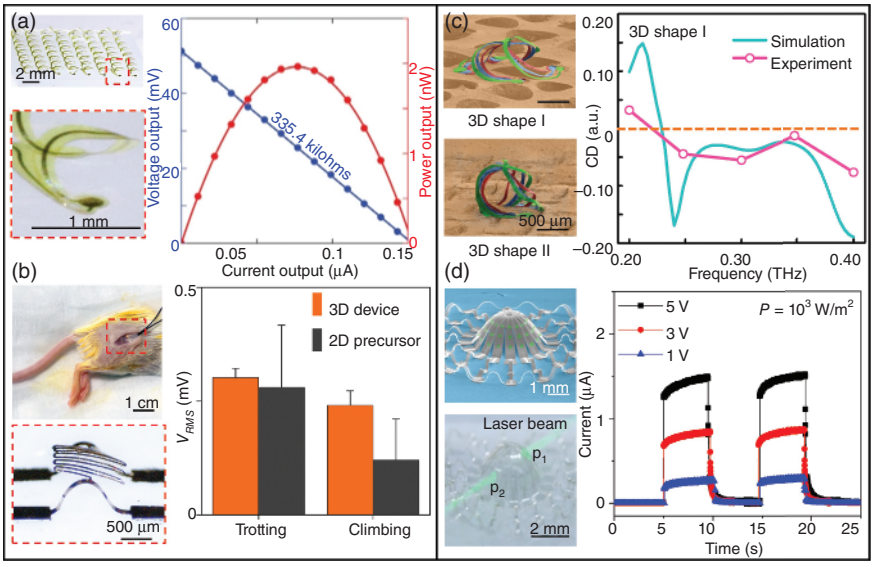

Figure 1.6 Applications of 3D mesostructures in energy harvesters and optics. (a) A 3D thermoelectric energy harvester with an array of 8×8 coils and the measured power output characteristics. Source: Nan et al. [66]/with permission of American Association for the Advancement of Science – AAAS. (b) A 3D piezoelectric energy harvester implanted into the hind leg of a mouse and the root-mean-square output voltages under different behaviors of the animal (e.g. trotting, climbing) in comparison to its 2D counterpart. Source: Han et al. [21]/with permission of Springer Nature. (c) SEM images of the 3D tunable optical chiral metamaterials with two unique 3D shapes based on the kirigami substrate, and the experimental and computational optical circular dichroism (CD) versus the frequency. Source: Zhao et al. [55]/with permission of National Academy of Sciences. (d) SEM and optical images of a 3D photodetector integrating 2D materials (graphene and MoS_2), and the photocurrent responses under the green laser illumination at different power densities. Source: Lee et al. [68]/with permission of Springer Nature.

geometries of the trilayer cage-like mesostructure (Shapes I and II), both of which have strongly chiral features. The distinct microscale configurations and the suitable physical scales (e.g. in-plane size <300 μm, ribbon width = 40 μm) trigger the mutually detuned resonant responses in the terahertz (THz) range. Simulation results and electromagnetic measurements under left-handed circularly polarized light (LCP) and right-handed circularly polarized light (RCP) show the phenomena of wavelength-dependent chirality and asymmetric absorption. Figure 1.6d shows a 3D photo-detecting device constructed with graphene and MoS_2 membranes [68]. The 3D hemispherical mesostructure with 16 ribbon components allows simultaneous detection of direction and intensity of the laser light. The time-resolved measurements at different bias voltages showed that the photo-detecting device can quickly switch between the "on" and "off" states as the laser changes. Based on the principles of geometric optics, the positions of entry and the exit points (P1, P2) of the laser on the 3D hemispherical surfaces can be determined by interpolating the photocurrent intensity.

1.6 Concluding Remarks

This chapter reviews the buckling-induced origami assembly methods, highlighting various design concepts, fabrication methods, applied materials, and device applications. The sophisticated 3D micro/nanostructures, determined by not only the layouts of 2D precursors, but also the deformable substrates and loading schemes, have compelling applications in different research fields, such as electronics, robotics, sensors, and optics. Although tremendous progress has been achieved in the assembly and application of 3D mesostructures, intractable challenges remain before realizing the full potential of the buckling assembly methods, thus providing fruitful opportunities for future explorations. One major challenge lies in the inverse design of 3D mesostructures due to the complicated nature of bifurcation and steric deformation of mechanical buckling process. The recently proposed topology optimization approaches, such as the moving morphable components method (MMC) [90] and the multiparameter genetic algorithm method (GA) [91], provide practical routes to the inverse designs of certain kirigami and filamentary mesostructures. The complex 3D structures with curved membrane features remain to be solved due to the much higher computational costs and the lack of straightforward mechanics models/algorithms. Besides, it is very important to further improve the manufacturing accuracy (e.g. positions, geometries, and dimensions) in the assembly process, as a significant step to the large-scale manufacturing of 3D mesostructures. With the further progress in the buckling methods and the applications, industrial-level and multifunctional devices can be expected in recent decades.

Acknowledgments

Y.Z. acknowledges support from the National Natural Science Foundation of China (#11672152 and #11722217), the Tsinghua National Laboratory for Information Science and Technology, and the State Key Laboratory of Digital Manufacturing Equipment and Technology, Huazhong University of Science and Technology (#DMETKF2019005).

References

1 Kim, D.-H. and Rogers, J.A. (2009). Bend, buckle, and fold: mechanical engineering with nanomembranes. *ACS Nano* 3 (3): 498–501.
2 Huang, G. and Mei, Y. (2012). Thinning and shaping solid films into functional and integrative nanomembranes. *Adv. Mater.* 24 (19): 2517–2546.
3 Liu, Z., Cui, A., Li, J., and Gu, C. (2019). Folding 2D structures into 3D configurations at the micro/nanoscale: principles, techniques, and applications. *Adv. Mater.* 31 (4): 1802211.

4 Ning, X., Wang, X., Zhang, Y. et al. (2018). Assembly of advanced materials into 3D functional structures by methods inspired by origami and kirigami: a review. *Adv. Mater. Interfaces* 5 (13): 1800284.

5 Xu, C., Wu, X., Huang, G., and Mei, Y. (2019). Rolled-up nanotechnology: materials issue and geometry capability. *Adv. Mater. Technol.* 4 (1): 1800486.

6 Rogers, J., Huang, Y., Schmidt, O.G., and Gracias, D.H. (2016). Origami MEMS and NEMS. *MRS Bull.* 41 (2): 123–129.

7 Huang, G. and Mei, Y. (2018). Assembly and self-assembly of nanomembrane materials-from 2D to 3D. *Small* 14 (14): 1703665.

8 Shulaker, M.M., Hills, G., Park, R.S. et al. (2017). Three-dimensional integration of nanotechnologies for computing and data storage on a single chip. *Nature* 547 (7661): 74.

9 Sharma, R., Bufon, C.C.B., Grimm, D. et al. (2014). Large-area rolled-up nanomembrane capacitor arrays for electrostatic energy storage. *Adv. Energy Mater.* 4 (9): 1301631.

10 Li, J., de Avila, B.E.-F., Gao, W. et al. (2017). Micro/nanorobots for biomedicine: delivery, surgery, sensing, and detoxification. *Sci. Rob.* 2 (4): eaam6431.

11 Li, X. (2011). Self-rolled-up microtube ring resonators: a review of geometrical and resonant properties. *Adv. Opt. Photonics* 3 (4): 366–387.

12 Randhawa, J.S., Gurbani, S.S., Keung, M.D. et al. (2010). Three-dimensional surface current loops in terahertz responsive microarrays. *Appl. Phys. Lett.* 96 (19): 191108.

13 Waldrop, M.M. (2016). The chips are down for Moore's law. *Nature* 530: 144–147.

14 Lee, B.-H., Kang, M.-H., Ahn, D.-C. et al. (2015). Vertically integrated multiple nanowire field effect transistor. *Nano Lett.* 15 (12): 8056–8061.

15 Gao, Y. (2016). The 'more Moore' and 'more than Moore' in microelectronics technology and IC industry. *Natl. Sci. Rev.* 3 (2): 158–158.

16 De Marchi, M., Sacchetto, D., Zhang, J. et al. (2014). Top-down fabrication of gate-all-around vertically stacked silicon nanowire FETs with controllable polarity. *IEEE Trans. Nanotechnol.* 13 (6): 1029–1038.

17 Kirihata, T., Golz, J., Wordeman, M. et al. (2016). Three-dimensional dynamic random access memories using through-silicon-vias. *IEEE J. Emerging Select. Topic Circuit Syst.* 6 (3): 373–384.

18 Cho, J.-H., Keung, M.D., Verellen, N. et al. (2011). Nanoscale origami for 3D optics. *Small* 7 (14): 1943–1948.

19 Yan, Z., Zhang, F., Liu, F. et al. (2016). Mechanical assembly of complex, 3D mesostructures from releasable multilayers of advanced materials. *Sci. Adv.* 2 (9): e1601014.

20 Zhang, F., Liu, F., and Zhang, Y. (2019). Analyses of mechanically-assembled 3D spiral mesostructures with applications as tunable inductors. *Sci. China-Technol. Sci.* 62 (2): 243–251.

21 Han, M., Wang, H., Yang, Y. et al. (2019). Three-dimensional piezoelectric polymer microsystems for vibrational energy harvesting, robotic interfaces and biomedical implants. *Nat. Electron.* 2 (1): 26–35.

22 Zhang, Y., Zhang, F., Yan, Z. et al. (2017). Printing, folding and assembly methods for forming 3D mesostructures in advanced materials. *Nat. Rev. Mater.* 2 (4): 17019.

23 Cheng, X. and Zhang, Y. (2019). Micro/nanoscale 3D assembly by rolling, folding, curving, and buckling approaches. *Adv. Mater.* 31 (36): e1901895.

24 Guo, X., Xue, Z., and Zhang, Y. (2019). Manufacturing of 3D multifunctional microelectronic devices: challenges and opportunities. *NPG Asia Mater.* 11: 29.

25 Schmidt, O.G. and Jin-Phillipp, N.Y. (2001). Free-standing SiGe-based nanopipelines on Si (001) substrates. *Appl. Phys. Lett.* 78 (21): 3310–3312.

26 Prinz, V.Y. (2003). A new concept in fabricating building blocks for nanoelectronic and nanomechanic devices. *Microelectron. Eng.* 69 (2–4): 466–475.

27 Mei, Y., Huang, G., Solovev, A.A. et al. (2008). Versatile approach for integrative and functionalized tubes by strain engineering of nanomembranes on polymers. *Adv. Mater.* 20 (21): 4085–4090.

28 Cui, A., Liu, Z., Li, J. et al. (2015). Directly patterned substrate-free plasmonic "nanograter" structures with unusual Fano resonances. *Light-Sci. Appl.* 4: e308.

29 Mao, Y., Pan, Y., Zhang, W. et al. (2016). Multi-direction-tunable three-dimensional meta-atoms for reversible switching between midwave and long-wave infrared regimes. *Nano Lett.* 16 (11): 7025–7029.

30 Legrain, A., Janson, T.G., Berenschot, J.W. et al. (2014). Controllable elastocapillary folding of three-dimensional micro-objects by through-wafer filling. *J. Appl. Phys.* 115 (21): 214905.

31 Cho, J.-H., Azam, A., and Gracias, D.H. (2010). Three dimensional nanofabrication using surface forces. *Langmuir* 26 (21): 16534–16539.

32 Py, C., Reverdy, P., Doppler, L. et al. (2007). Capillary origami: spontaneous wrapping of a droplet with an elastic sheet. *Phys. Rev. Lett.* 98 (15): 156103.

33 Iwase, E. and Shimoyama, I. (2005). Multistep sequential batch assembly of three-dimensional ferromagnetic microstructures with elastic hinges. *J. Microelectromech. Syst.* 14 (6): 1265–1271.

34 In, H.J., Lee, H., Nichol, A.J. et al. (2008). Carbon nanotube-based magnetic actuation of origami membranes. *J. Vac. Sci. Technol., B* 26 (6): 2509–2512.

35 Kuribayashi-Shigetomi, K., Onoe, H., and Takeuchi, S. (2012). Cell origami: self-folding of three-dimensional cell-laden microstructures driven by cell traction force. *PLoS One* 7 (12): e51085.

36 Pandey, S., Ewing, M., Kunas, A. et al. (2011). Algorithmic design of self-folding polyhedra. *Proc. Natl. Acad. Sci. U.S.A.* 108 (50): 19885–19890.

37 Huang, W., Koric, S., Yu, X. et al. (2014). Precision structural engineering of self-rolled-up 3D nanomembranes guided by transient quasi-static FEM modeling. *Nano Lett.* 14 (11): 6293–6297.

38 Choi, C., Choi, M.K., Liu, S. et al. (2017). Human eye-inspired soft optoelectronic device using high-density MoS_2-graphene curved image sensor array. *Nat. Commun.* 8: 1664.

39 Kim, D.-H., Lu, N., Ghaffari, R. et al. (2011). Materials for multifunctional balloon catheters with capabilities in cardiac electrophysiological mapping and ablation therapy. *Nat. Mater.* 10 (4): 316–323.

40 Song, Y.M., Xie, Y., Malyarchuk, V. et al. (2013). Digital cameras with designs inspired by the arthropod eye. *Nature* 497 (7447): 95–99.

41 Xue, Z., Song, H., Rogers, J.A. et al. (2019). Mechanically-guided structural designs in stretchable inorganic electronics. *Adv. Mater.* 32: e1902254.

42 Ko, H.C., Shin, G., Wang, S. et al. (2009). Curvilinear electronics formed using silicon membrane circuits and elastomeric transfer elements. *Small* 5 (23): 2703–2709.

43 Ko, H.C., Stoykovich, M.P., Song, J. et al. (2008). A hemispherical electronic eye camera based on compressible silicon optoelectronics. *Nature* 454 (7205): 748–753.

44 Saada, G., Layani, M., Chernevousky, A., and Magdassi, S. (2017). Hydroprinting conductive patterns onto 3D structures. *Adv. Mater. Technol.* 2 (5): 1600289.

45 Le Borgne, B., De Sagazan, O., Crand, S. et al. (2017). Conformal electronics wrapped around daily life objects using an original method: water transfer printing. *ACS Appl. Mater. Interfaces* 9 (35): 29424–29429.

46 Xu, X., Davanco, M., Qi, X., and Forrest, S.R. (2008). Direct transfer patterning on three dimensionally deformed surfaces at micrometer resolutions and its application to hemispherical focal plane detector arrays. *Org. Electron.* 9 (6): 1122–1127.

47 Fan, D., Lee, B., Coburn, C., and Forrest, S.R. (2019). From 2D to 3D: strain- and elongation-free topological transformations of optoelectronic circuits. *Proc. Natl. Acad. Sci. U.S.A.* 116 (10): 3968–3973.

48 Park, H., Cho, H., Kim, J. et al. (2014). Multiscale transfer printing into recessed microwells and on curved surfaces via hierarchical perfluoropolyether stamps. *Small* 10 (1): 52–59.

49 Xu, S., Yan, Z., Jang, K.-I. et al. (2015). Assembly of micro/nanomaterials into complex, three-dimensional architectures by compressive buckling. *Science* 347 (6218): 154–159.

50 Yan, Z., Han, M., Yang, Y. et al. (2017). Deterministic assembly of 3D mesostructures in advanced materials via compressive buckling: a short review of recent progress. *Extreme Mech. Lett.* 11: 96–104.

51 Yan, Z., Zhang, F., Wang, J. et al. (2016). Controlled mechanical buckling for origami-inspired construction of 3d microstructures in advanced materials. *Adv. Funct. Mater.* 26 (16): 2629–2639.

52 Zhang, Y., Yan, Z., Nan, K. et al. (2015). A mechanically driven form of kirigami as a route to 3D mesostructures in micro/nanomembranes. *Proc. Natl. Acad. Sci. U.S.A.* 112 (38): 11757–11764.

53 Luan, H., Cheng, X., Wang, A. et al. (2019). Design and fabrication of heterogeneous, deformable substrates for the mechanically guided 3D assembly. *ACS Appl. Mater. Interfaces* 11 (3): 3482–3492.

54 Nan, K., Luan, H., Yan, Z. et al. (2017). Engineered elastomer substrates for guided assembly of complex 3D mesostructures by spatially nonuniform compressive buckling. *Adv. Funct. Mater.* 27 (1): 1604281.

55 Zhao, H., Li, K., Han, M. et al. (2019). Buckling and twisting of advanced materials into morphable 3D mesostructures. *Proc. Natl. Acad. Sci. U.S.A.* 116: 201901193.

56 Fu, H., Nan, K., Bai, W. et al. (2018). Morphable 3D mesostructures and microelectronic devices by multistable buckling mechanics. *Nat. Mater.* 17 (3): 268–276.

57 Guo, X., Wang, X., Ou, D. et al. (2018). Controlled mechanical assembly of complex 3D mesostructures and strain sensors by tensile buckling. *NPJ Flexible Electron.* 2 (1): 14.

58 Kim, B.H., Lee, J., Won, S.M. et al. (2018). Three-dimensional silicon electronic systems fabricated by compressive buckling process. *ACS Nano* 12 (5): 4164–4171.

59 Kim, B.H., Liu, F., Yu, Y. et al. (2018). Mechanically guided post-assembly of 3D electronic systems. *Adv. Funct. Mater.* 28 (48): 1803149.

60 Yan, Z., Han, M., Shi, Y. et al. (2017). Three-dimensional mesostructures as high-temperature growth templates, electronic cellular scaffolds, and self-propelled microrobots. *Proc. Natl. Acad. Sci. U.S.A.* 114 (45): E9455–E9464.

61 Ning, X., Yu, X., Wang, H. et al. (2018). Mechanically active materials in three-dimensional mesostructures. *Sci. Adv.* 4 (9): eaat8313.

62 Nan, K., Wang, H., Ning, X. et al. (2019). Soft three-dimensional microscale vibratory platforms for characterization of nano-thin polymer films. *ACS Nano* 13 (1): 449–457.

63 Fu, H., Nan, K., Froeter, P. et al. (2017). Mechanically-guided deterministic assembly of 3D mesostructures assisted by residual stresses. *Small* 13: 1700151.

64 McCracken, J.M., Xu, S., Badea, A. et al. (2017). Deterministic integration of biological and soft materials onto 3D microscale cellular frameworks. *Adv. Biosyst.* 1 (9): 1700068.

65 Jang, K.-I., Li, K., Chung, H.U. et al. (2017). Self-assembled three dimensional network designs for soft electronics. *Nat. Commun.* 8: 15894.

66 Nan, K., Kang, S.D., Li, K. et al. (2018). Compliant and stretchable thermoelectric coils for energy harvesting in miniature flexible devices. *Sci. Adv.* 4 (11): eaau5849.

67 Yang, C., Huang, Y., Cheng, H. et al. (2019). Rollable, stretchable, and reconfigurable graphene hygroelectric generators. *Adv. Mater.* 31 (2): 1805705.

68 Lee, W., Liu, Y., Lee, Y. et al. (2018). Two-dimensional materials in functional three-dimensional architectures with applications in photodetection and imaging. *Nat. Commun.* 9: 1417.

69 Shi, Y., Zhang, F., Nan, K. et al. (2017). Plasticity-induced origami for assembly of three dimensional metallic structures guided by compressive buckling. *Extreme Mech. Lett.* 11: 105–110.

70 Zhang, F., Fan, Z., and Zhang, Y. (2018). A theoretical model of postbuckling in straight ribbons with engineered thickness distributions for three-dimensional assembly. *Int. J. Solids Struct.* 147: 254–271.

71 Luo, G., Fu, H., Cheng, X. et al. (2019). Mechanics of bistable cross-shaped structures through loading-path controlled 3D assembly. *J. Mech. Phys. Solids* 129: 261–277.

72 Humood, M., Shi, Y., Han, M. et al. (2018). Fabrication and deformation of 3D multilayered kirigami microstructures. *Small* 14: 1703852.

73 Liu, Y., Yan, Z., Lin, Q. et al. (2016). Guided formation of 3D helical mesostructures by mechanical buckling: analytical modeling and experimental validation. *Adv. Funct. Mater.* 26 (17): 2909–2918.

74 Liu, Y., Xu, Z., Hwang, K.C. et al. (2019). Postbuckling analyses of frame mesostructures consisting of straight ribbons for mechanically guided three-dimensional assembly. *Proc. Math. Phys. Eng. Sci.* 475 (2225): 20190012.

75 Fan, Z., Hwang, K.-C., Rogers, J.A. et al. (2018). A double perturbation method of postbuckling analysis in 2D curved beams for assembly of 3D ribbon-shaped structures. *J. Mech. Phys. Solids* 111: 215–238.

76 Ling, Y., Zhuang, X., Xu, Z. et al. (2018). Mechanically assembled, three-dimensional hierarchical structures of cellular graphene with programmed geometries and outstanding electromechanical properties. *ACS Nano* 12 (12): 12456–12463.

77 Wang, X., Guo, X., Ye, J. et al. (2019). Freestanding 3D mesostructures, functional devices, and shape-programmable systems based on mechanically induced assembly with shape memory polymers. *Adv. Mater.* 31 (2): 1805615.

78 Park, Y., Luan, H., Kwon, K. et al. (2019). Transformable, freestanding 3D mesostructures based on transient materials and mechanical interlocking. *Adv. Funct. Mater.* 29: 1903181.

79 Liu, F., Chen, Y., Song, H. et al. (2019). High performance, tunable electrically small antennas through mechanically guided 3D assembly. *Small* 15 (1): 1804055.

80 Liu, F., Cheng, X., Zhang, F. et al. (2019). Design and assembly of reconfigurable 3D radio-frequency antennas based on mechanically triggered switches. *Adv. Electron. Mater.* 5 (6): 1900256.

81 Won, S.M., Wang, H., Kim, B.H. et al. (2019). Multimodal sensing with a three-dimensional piezoresistive structure. *ACS Nano* 13: 10972.

82 Guo, X., Xu, Z., Zhang, F. et al. (2018). Reprogrammable 3D mesostructures through compressive buckling of thin films with prestrained shape memory polymer. *Acta Mech. Solida Sin.* 31 (5): 589–598.

83 Shi, Y., Pei, P., Cheng, X. et al. (2018). An analytic model of two-level compressive buckling with applications in the assembly of free-standing 3D mesostructures. *Soft Matter* 14 (43): 8828–8837.

84 Wang, H., Ning, X., Li, H. et al. (2018). Vibration of mechanically-assembled 3D microstructures formed by compressive buckling. *J. Mech. Phys. Solids* 112: 187–208.

85 Li, H., Wang, X., Zhu, F. et al. (2018). Viscoelastic characteristics of mechanically assembled three-dimensional structures formed by compressive buckling. *J. Appl. Mech.* 85 (12): 121002.

86 Ning, X., Wang, H., Yu, X. et al. (2017). 3D tunable, multiscale, and multistable vibrational micro-platforms assembled by compressive buckling. *Adv. Funct. Mater.* 27: 1605914.

87 Li, K., Cheng, X., Zhu, F. et al. (2019). A generic soft encapsulation strategy for stretchable electronics. *Adv. Funct. Mater.* 29 (8): 1806630.

88 Li, S., Han, M., Rogers, J.A. et al. (2019). Mechanics of buckled serpentine structures formed via mechanics-guided, deterministic three-dimensional assembly. *J. Mech. Phys. Solids* 125: 736–748.

89 Liu, Y., Wang, X., Xu, Y. et al. (2019). Harnessing the interface mechanics of hard films and soft substrates for 3D assembly by controlled buckling. *Proc. Natl. Acad. Sci. U.S.A.* 116 (31): 15368–15377.

90 Xue, R., Li, R., Du, Z. et al. (2017). Kirigami pattern design of mechanically driven formation of complex 3D structures through topology optimization. *Extreme Mech. Lett.* 15: 139–144.

91 Xu, Z., Fan, Z., Fu, H. et al. (2019). Optimization-based approach for the inverse design of ribbon-shaped three-dimensional structures assembled through compressive buckling. *Phys. Rev. Appl.* 11 (5): 054053.